nature nanotechnology

LETTERS

PUBLISHED ONLINE: 23 JUNE 2013 | DOI: 10.1038/NNANO.2013.104

Readout and control of a single nuclear spin with a metastable electron spin ancilla

Sang-Yun Lee[1‡], Matthias Widmann[1], Torsten Rendler[1], Marcus W. Doherty[2*], Thomas M. Babinec[3†], Sen Yang[1], Moritz Eyer[1], Petr Siyushev[1], Birgit J. M. Hausmann[3], Marko Loncar[3], Zoltán Bodrog[4], Adam Gali[4,5], Neil B. Manson[2], Helmut Fedder[1‡*] and Jörg Wrachtrup[1]

Electron and nuclear spins associated with point defects in insulators are promising systems for solid-state quantum technology[1–3]. The electron spin is usually used for readout and addressing, and nuclear spins are used as exquisite quantum bits[4,5] and memory systems[3,6]. With these systems, single-shot readout of single nuclear spins[5,7] as well as entanglement[4,8,9], aided by the electron spin, have been shown. Although the electron spin in this example is essential for readout, it usually limits the nuclear spin coherence[10], leading to a quest for defects with spin-free ground states[9,11]. Here, we isolate a hitherto unidentified defect in diamond and use it at room temperature to demonstrate optical spin polarization and readout with exceptionally high contrast (up to 45%), coherent manipulation of an individual excited triplet state spin, and coherent nuclear spin manipulation using the triplet electron spin as a metastable ancilla. We demonstrate nuclear magnetic resonance and Rabi oscillations of the uncoupled nuclear spin in the spin-free electronic ground state. Our study demonstrates that nuclei coupled to single metastable electron spins are useful quantum systems with long memory times, in spite of electronic relaxation processes.

Coupled electron and nuclear spins in solids are promising candidates for use in quantum memories and registers and form a particular class in the emerging field of hybrid quantum systems[8,12–15], in which different types of qubit perform distinct functions according to their advantageous properties. In this particular case, the nuclear spin, which is weakly coupled to the environment, serves as a long-lived quantum memory, whereas the electron spin, which has a short coherence time but interacts strongly with external fields, serves as a readout gate[4,8,10]. In this architecture, the permanent presence of the electron spin is a source of decoherence for the nuclear spin[9]. To avoid such electron-spin-induced decoherence, the electron that carries the spin should be physically removed when it is not needed and returned to the nuclear spin only when the initialization or readout gate is applied. One approach to address this problem is to remove the electron frequently, for example by photo-ionization with a strong laser, resulting in a motional narrowing type of decoupling[10]. Another approach—one that is followed in this work—is to choose an electronic system with a spin-free ground state and a metastable excited spin state that can be optically pumped and activated before application of the readout gate[9]. Such a system implemented with a single solid-state defect would provide a universal nuclear spin gate. In the following we present a suitable defect in diamond and demonstrate coherent control of a single nuclear spin in the spin-free electronic ground state. Notably, as well as the nitrogen–vacancy (NV) centre, this is the second known single spin defect in the solid state, the coherent spin motion of which is detectable at room temperature.

The defect (hereafter termed the ST1 defect following the convention commonly applied by the electron spin resonance (ESR) community) was observed in ultrapure single-crystalline high-pressure, high-temperature (HPHT) diamond after the fabrication of vertical nanowires (Fig. 1a,b), the main purpose of which is to provide high photon collection efficiency[16]. The wires were etched into the sample surface by reactive ion etching (Supplementary Section S2). Figure 1c presents a confocal fluorescence microscope image of the sample. To identify candidates for metastable triplet spin defects, we examined the fluorescence intensity of bright spots on the sample surface with and without a strong applied magnetic field (from a permanent magnet, ~0.5 T) (Fig. 1d). An arbitrarily oriented magnetic field causes spin mixing and thereby modifies the steady-state fluorescence[17]. We can see two types of emitters with decreasing and increasing fluorescence response, corresponding to NV^- centres and the new ST1 defects, respectively. The increase in the steady-state fluorescence is due to mixing of metastable triplet states, as will be shown in the following.

To characterize the defect further, we recorded the photon autocorrelation and observed a dip well below 0.5 at zero delay, which confirms that we indeed observe single defects[18] (Fig. 1g). At higher excitation intensity, the photon autocorrelation shows pronounced 'bunching-shoulders', which supports the idea of the existence of a long-lived shelving state. To characterize the defect fluorescence, we present fluorescence emission spectra at room temperature and at 10 K (Fig. 1e). In both cases, a strong resonant emission line is observed at 550(1) nm, with a broad phonon side band extending to the near-infrared. Notably, this resonant transition does not correspond to a known diamond defect line[19]. To characterize the strength of the optical transition, we present the excited-state lifetime, which we determined in a room-temperature experiment using pulsed optical excitation (Fig. 1f). An excited state lifetime of 9.5(2) ns was obtained.

We next searched for a signature of an ESR in the optical fluorescence. Figure 2a shows the fluorescence intensity that is observed while sweeping the microwaves from 200 MHz to 1,400 MHz. Three

[1]3. Physikalisches Institut and Research Center SCOPE, University Stuttgart, Pfaffenwaldring 57, 70569 Stuttgart, Germany, [2]Laser Physics Centre, Research School of Physics and Engineering, Australian National University, Canberra, ACT 0200, Australia, [3]School of Engineering and Applied Science, Harvard University, Cambridge, Massachusetts 02138, USA, [4]Wigner Research Centre for Physics, Hungarian Academy of Sciences, PO Box 1525, Budapest, Hungary, [5]Department of Atomic Physics, Budapest University of Technology and Economics, Budafoki út 8, H-1111, Budapest, Hungary; [†]Present address: Department of Applied Physics, Stanford University, 348 Via Pueblo Mall, Stanford, California 94305, USA; [‡]These authors contributed equally to this work. *e-mail: helmut.fedder@gmail.com; marcus.doherty@anu.edu.au

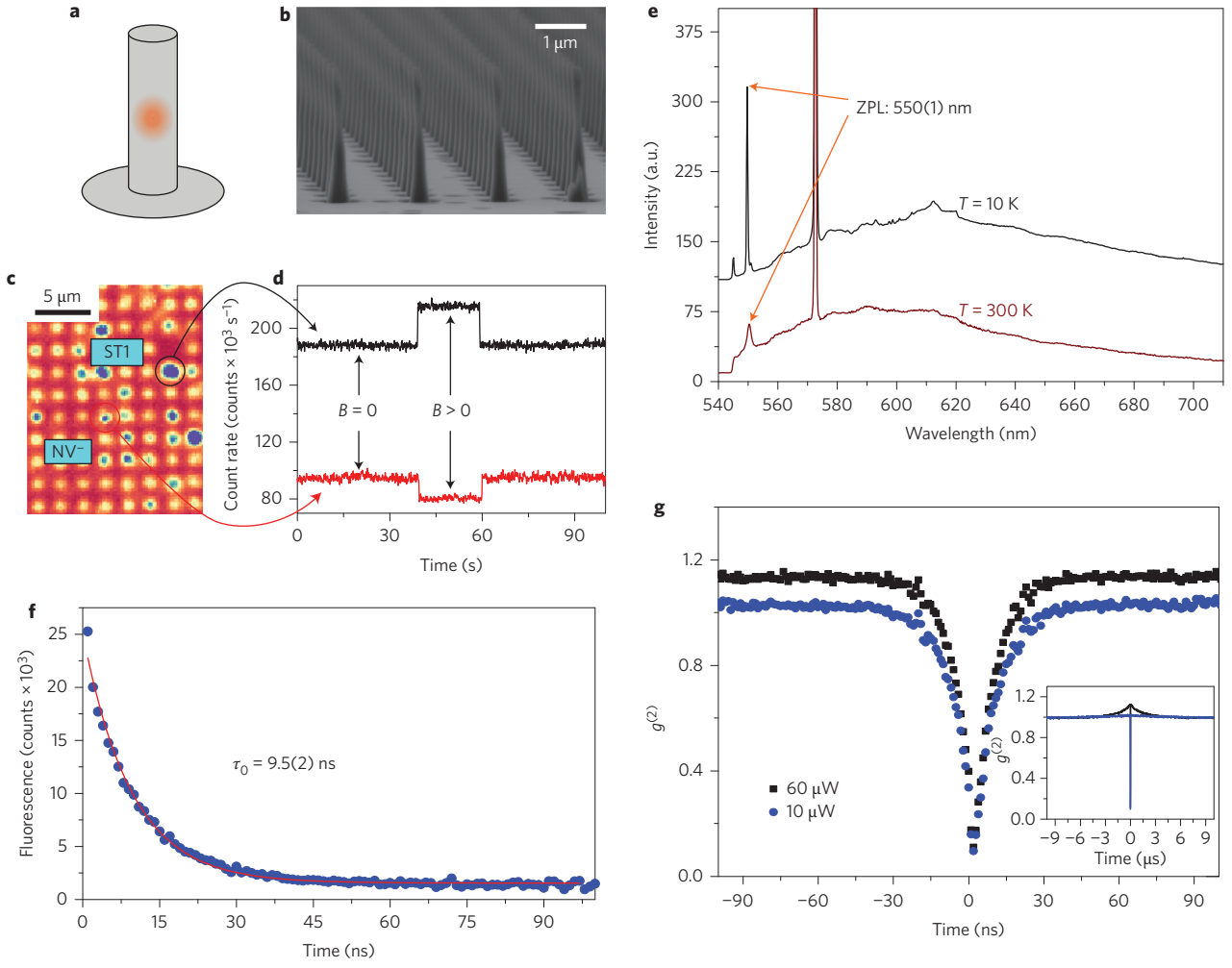

Figure 1 | Optical properties of the ST1 defect. a, Schematic of a diamond nanowire containing a single fluorescent point defect. **b**, Scanning electron microscopy image of the [111] HPHT diamond sample with fabricated nanowires (diameter, ~200 nm; length, ~2 μm). **c**, Confocal fluorescence microscope image of the sample. The indicated wires contain single NV^- and ST1 defects. **d**, Fluorescence time trace recorded during application and removal of a non-aligned magnetic field. The fluorescence is quenched and enhanced for NV^- and ST1 defects, respectively. **e**, Fluorescence emission spectrum of a single ST1 defect at room temperature and liquid-helium temperature. A zero phonon line at 550(1) nm and a broad emission band in the red to near-infrared range is observed. The sharp peak at 573 nm is due to inelastic Raman scattering of the 532 nm excitation laser. **f**, Fluorescence decay showing an excited-state lifetime of 9.5(2) ns. **g**, Second-order photon correlation at increasing excitation power. The dip at delay $t = 0$ reaches well below 0.5, proving the single centre nature of the defect. The inset shows the full data set acquired over a time range of 10 μs. At high excitation power, pronounced bunching shoulders with a time constant of ~2 μs are observed (black line in the inset), indicating the presence of a long-lived shelving state.

distinct lines marking an increase in fluorescence intensity upon spin resonance are observed at frequencies $2E = 278(1)$ MHz, $D - E = 996(1)$ MHz and $D + E = 1{,}274(1)$ MHz. This optically detected magnetic resonance (ODMR) spectrum indicates a triplet electron spin with zero field splitting parameters[20] $D = 1{,}135(1)$ MHz and $E = 139(1)$ MHz. The observed large E parameter could originate from the presence of a large local strain or from an intrinsic low symmetry of the defect. We compared the spin resonance spectra of ~20 individual defects (Supplementary Section S5) and observed variations of the E parameter smaller than 5 MHz, indicating that the E indeed originates from the intrinsic low symmetry of the defect. From ODMR spectra obtained when a variable axial magnetic field was applied (Fig. 2b), we determine an electronic g-factor of $g_e = 2.0(1)$, close to the g-factor of the free-electron spin. The absence of an intrinsic hyperfine splitting indicates that the defect's constituent atoms have no nuclear spin (see Supplementary Section S7 for a detailed discussion of the possible constituents and structure of the defect). The aligned axial magnetic field has an angle of 35(1)° with respect to the [111] crystal direction, indicating that the defect's main symmetry axis is oriented along the [110] crystal direction (see inset in Fig. 2b).

All our findings reported so far are compatible with two possible electronic configurations: the triplet state could either be the long-lived shelving state or the ground state. To show that the triplet state is indeed the long-lived shelving state, we measured the decay of the shelving-state population. If the shelving state was a singlet, a single exponential decay would be expected. In contrast, in the present case, three distinct exponential decay terms are observed (Fig. 3b) and their amplitudes are sensitive to microwave fields resonant with the triplet ESR transitions. In each decay curve shown, the dominant decay terms are controlled by switching the spin population with microwave π-pulses resonant with the three ESR transitions. This indicates that the shelving state is indeed the triplet state. The result can be used to assign the decay constants to the spin quantum numbers (Fig. 3c). A complete model of the optical cycle can be established by also determining the triplet population rate using an analogous pulsed experiment (Supplementary Section S4.3). Figure 3d

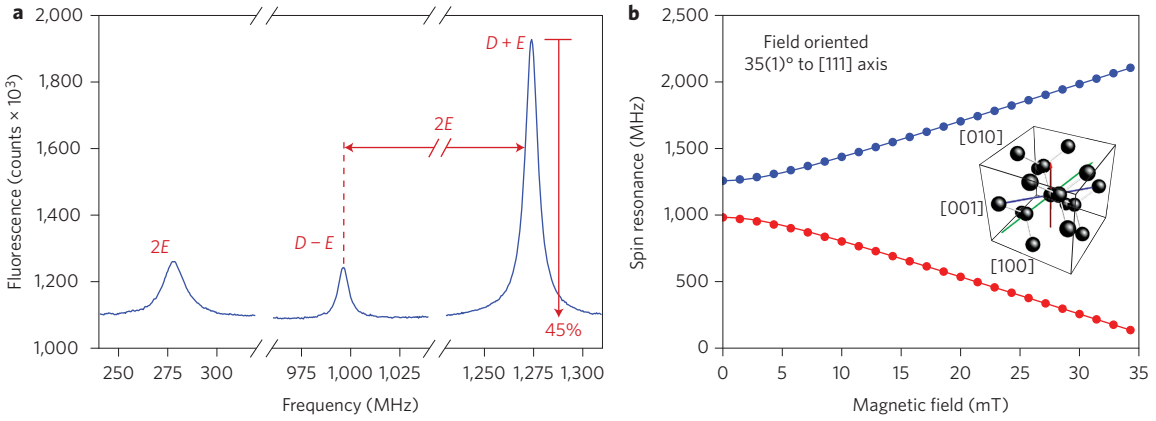

Figure 2 | Optically detected electron spin resonance. a, Room-temperature ESR spectrum at zero magnetic field. Resonant transitions are indicated by their zero-field splitting parameters $D = 1{,}135(1)$ MHz and $E = 139(1)$ MHz. We observe an exceptionally high optical spin signal contrast of the $D + E$ spin projection of ~45%. **b**, Zeeman curve with an aligned axial magnetic field oriented along the defect main symmetry axis (35(1)° with respect to the [111] crystal axis). Symbols, experiment; lines, theoretical fit obtained from the triplet spin Hamiltonian $H = D[S_z^2 - S(S+1)/3] + E(S_x^2 - S_y^2) + gS_zB_z$, where S_α are the usual spin operators for total spin $S = 1$, g is the g-factor, and B_z is the axial field (Supplementary Section S5). Inset: schematic illustration of the crystallographic orientation of the defect. Green, blue and red arrows denote [111], [110] (defect's main axis) and [001] (C_{2v} symmetry axis), respectively.

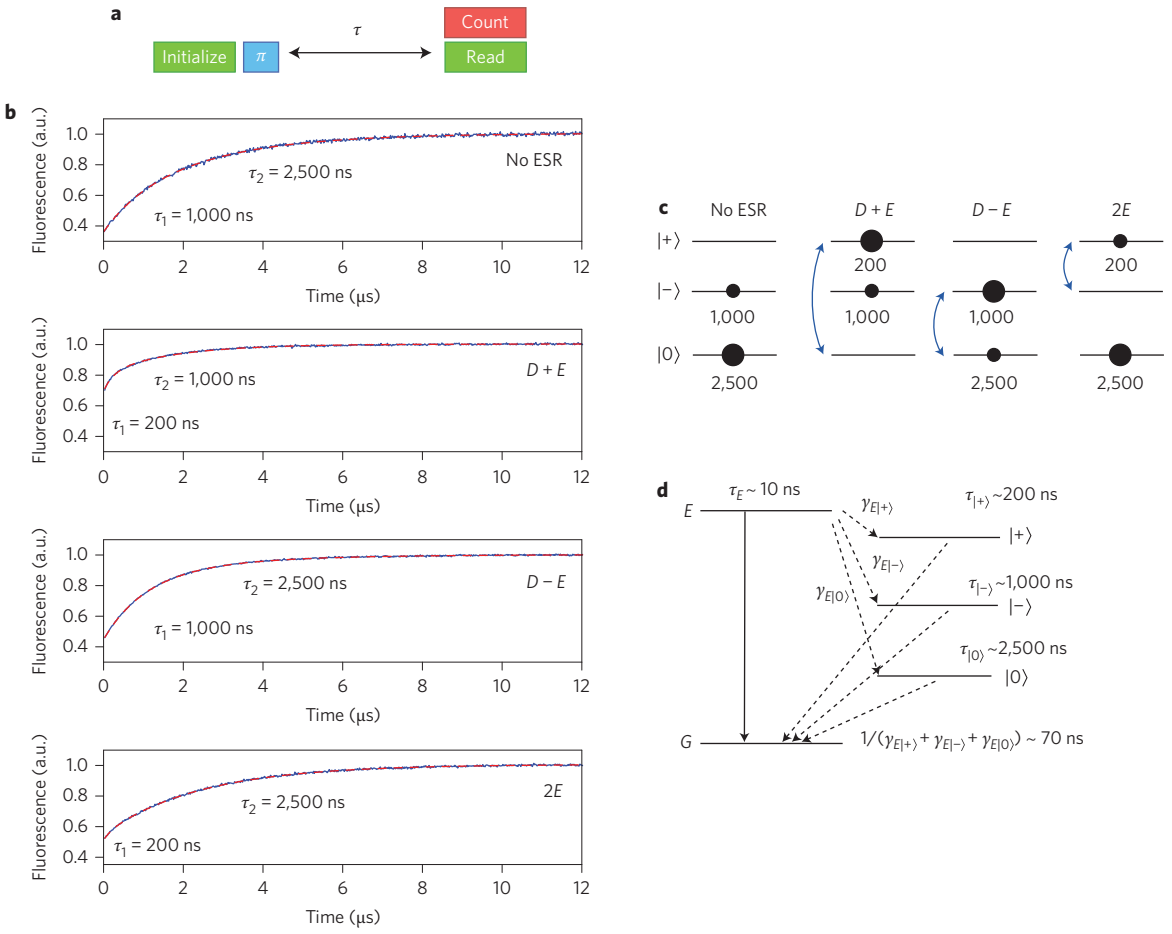

Figure 3 | Kinetics of the shelving state and energy-level scheme at zero magnetic field. a, Optical and microwave pulse sequence for measurement of shelving-state lifetimes. After an optical pump pulse, a resonant microwave π-pulse is applied to exchange the populations of selected spin sublevels and thereby control the dominant decay constants. **b**, Decay curves of the shelving-state population described by double exponential functions $y = c - a_1 \exp(-t/\tau_1) - a_2 \exp(-t/\tau_2)$. Blue, experimental data; red dashes, double exponential fits (Supplementary Section S4.2). For each panel, the microwave π-pulse is resonant with the denoted ESR transition. **c**, Assignment of the decay constants to the triplet energy levels. The initial populations (no ESR) are proportional to the decay constants. The small population of the short-lived state is omitted. The observed decay constants imply the assignment of the energy levels denoted on the left. **d**, Summary of the triplet kinetics and electronic structure consisting of singlet ground and excited states and a metastable triplet state. Transition rates between two states i and j and the lifetime of a state i are denoted γ_{ij} and τ_i, respectively.

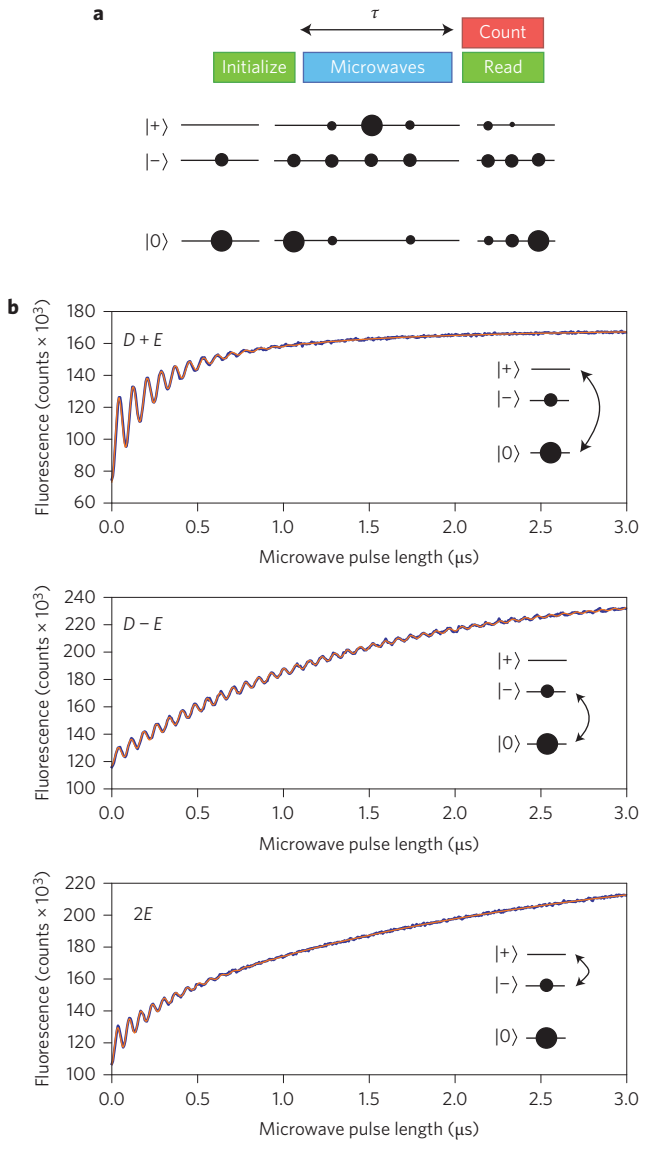

Figure 4 | Coherent triplet spin manipulation. a, Optical and microwave pulse sequence and evolution of the triplet populations (here illustrated for microwaves resonant with the $D+E$ transition). **b**, Rabi oscillations among the triplet spin sublevels at zero magnetic field. Thick blue lines show experimental data, thin red lines show theoretical fits with the model $I = I_0 - (a_1 + a_2 \cos \Omega t) \exp(-t/\bar{\tau}) - a_3 \exp(t/\tau)$, where $\bar{\tau} = 2(\tau_\alpha^{-1} + \tau_\beta^{-1})^{-1}$ is a combined decay constant of the levels α and β involved in the Rabi oscillations, τ is the decay constant of the remaining level, a_i are fluorescence amplitudes and Ω is the Rabi frequency. Note that for the top and bottom panel the combined decay constant is dominated by the fast decay of the $|+\rangle$ level. For the fit shown in the middle panel the last term is omitted, because the unaffected level is the $|+\rangle$ level, which is (nearly) unpopulated.

summarizes all results related to the triplet kinetics. The essential features are a rapid ($\sim$1/70 ns) intersystem crossing rate from the singlet excited state to the triplet state and substantial differences among the triplet lifetimes ($\tau_{|0\rangle} \approx 2{,}500$ ns, $\tau_{|-\rangle} \approx 1{,}000$ ns, $\tau_{|+\rangle} \approx 200$ ns). These are responsible for the positive and exceptionally high (45%) optical spin signal contrast, and the increasing steady-state fluorescence response to a randomly aligned static magnetic field, as observed in Fig. 1d, because mixing the triplet sublevels results in faster decay to the ground state. It follows that optical pumping prepares the system in a spin-polarized state of the metastable triplet state with a predominant population in the slowly decaying triplet sublevel, $|0\rangle$.

We then applied coherent spin manipulation to demonstrate Rabi oscillations between the triplet spin states (Fig. 4). Because the spin population of the faster decaying states $|+\rangle$ or $|-\rangle$ is increased by a resonant ESR pulse, any coherent spin manipulation results in enhancement of the fluorescence intensity, as shown in Fig. 4b. The oscillations are described by two exponential decay functions, one of which is modulated by a cosine. The decay times and oscillation amplitudes correspond to the average of the lifetimes and the difference between the initial populations of the two involved spin states, respectively, and are in excellent agreement with the rates measured independently above (Fig. 3d). Note that the decay times are fully accounted for by the triplet lifetimes, which implies that spin relaxation is negligible. The triplet lifetimes are long enough to coherently address a coupled nuclear spin. We compared the Zeeman sweeps of about 20 defects and observed that two of them show hyperfine splittings due to proximal $I = 1/2$ carbon nuclear spins of several tens of megahertz (Fig. 5a).

The metastable electron spin was then exploited for the initialization and readout of the nuclear spin in the spin-free electronic ground state. To achieve this, we used the metastable electronic triplet spin ancilla to transfer spin-polarization onto and off the nuclear spin. To this end, the optical nuclear polarization (ONP) induced by a level anticrossing (LAC) between the $|-1, +1/2\rangle$ and $|0, -1/2\rangle$ hyperfine levels at $\sim$42 mT was used to selectively mix electronic and nuclear spin states[20,21] (Supplementary Sections S6 and S8). Under these conditions, spin-polarization is transferred to the nuclear spin when the electron enters the metastable triplet level, resulting in optical polarization of the nuclear spin[22]. After the optical pump pulse is turned off, the electron decays to the singlet ground state within a time given by the triplet lifetime. This decay eliminates the triplet electron spin and leaves the nuclear spin in its polarized state. Similarly, when the system is optically pumped from the singlet ground state to the excited triplet state, the nuclear spin state is preserved and the hyperfine levels are populated correspondingly. At the LAC, the different lifetimes of the hyperfine levels result in different fluorescent intensities of the nuclear spin projections. This provides a mechanism to read out the nuclear spin (see Fig. 5b and Methods). Figure 5c shows the nuclear spin signal contrast as the energy levels are tuned into the LAC. Nuclear spin polarization is maximal at the LAC and vanishes when the detuning from the LAC becomes comparable to the hyperfine coupling strength. At the centre of the LAC, the signal contrast is $\sim$1.4%. This observed contrast is slightly below the expectations from a ten-level rate model of the optical cycles that accounts for the mixed hyperfine levels, and predicts a signal contrast of $\sim$4% with inverse sign. Given the observed ESR transition strengths at the LAC, we tentatively attribute this sign change to the readout contrast; however, a more detailed model is required to account for the precise ONP signal strength (Supplementary Section S8).

To demonstrate an application of nuclear spin manipulation, Fig. 5d,e presents nuclear magnetic resonance (NMR) and coherent manipulation of the nuclear spin via Rabi oscillations . To measure an NMR spectrum, we applied a radiofrequency π-pulse of variable frequency. A resonance dip can be observed at 450(1) kHz (Fig. 5d), which corresponds to the Larmor precession frequency $\nu_{^{13}C} = \gamma_{^{13}C} B = 447(5)$ kHz for a bare ^{13}C nucleus. Here, $\gamma_{^{13}C} = 10.705$ kHz mT^{-1} is the gyromagnetic ratio of the ^{13}C nuclear spin and $B = 41.8(5)$ mT is the applied field (corresponding to the LAC). We can thereby identify the coupled nuclear spin as a ^{13}C lattice spin. Note the absence of a chemical shift, which indicates that the electron spin is indeed absent. To measure nuclear Rabi oscillations, we applied a resonant radiofrequency pulse of variable length between the initialization and

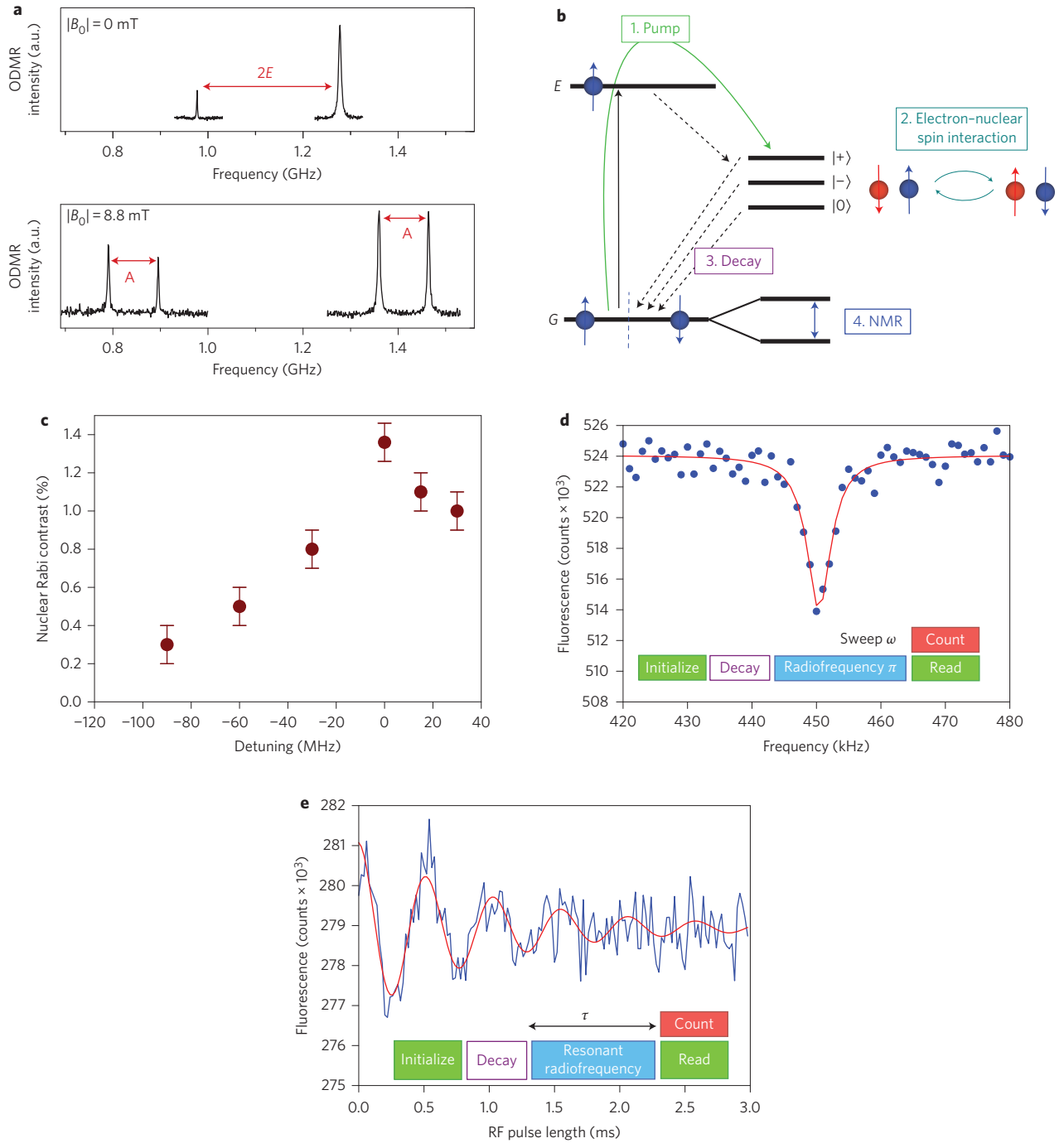

Figure 5 | Readout and control of a single nuclear spin in the spin-free electronic ground state. a, ODMR spectra of an ST1 defect with a nearby ^{13}C nuclear spin, under zero (top panel) and moderate (bottom panel) magnetic field applied along the axis of the defect. *E* and *A* denote the zero-field and hyperfine splitting parameters, respectively. The hyperfine splitting is suppressed at small fields and becomes visible when the Zeeman energy is larger than the *E* parameter. **b**, Readout and control of the nuclear spin with the electronic triplet spin ancilla. The nuclear spin (blue arrows) is interrogated by optically pumping the electron spin (red arrows) into the triplet state and allowing the electron and nuclear spin to interact. The subsequent decay of the triplet state destroys the electron spin and leaves the nuclear spin unchanged. The bare nuclear spin is then coherently manipulated by NMR. Efficient transfer of spin polarization between the electron and nuclear spin in the triplet state is provided by exploiting an ONP as a consequence of LAC between the $|-1,+1/2\rangle$ and $|0,-1/2\rangle$ hyperfine levels (see main text). **c**, Signal contrast of nuclear Rabi oscillations, corresponding to the product of the nuclear spin polarization and readout contrast, as a function of detuning from the LAC (zero detuning corresponds to the LAC). For the determination of the error bars, see Methods. **d**,**e**, NMR spectrum and Rabi oscillations of the nuclear spin in the electronic ground state. For the NMR spectrum (**d**), a radiofrequency π-pulse of variable frequency is inserted between the preparation and readout laser pulses. The resonance dip corresponds to the Larmor precession of a bare ^{13}C nuclear spin. Blue, experimental data; red, Lorentzian fit. Note that the NMR line width (4.5(2) kHz, obtained from the Lorentzian fit) is determined by power broadening and in the present case of a pulsed measurement corresponds approximately to the inverse radiofrequency π-pulse width (0.2 ms). For the Rabi oscillations (**e**), a resonant radiofrequency pulse of variable length is inserted between the initialization and readout laser pulses. Blue, experimental data; red, exponentially decaying cosine fit; decay constant 1.0(1) ms.

readout laser pulses. Several Rabi oscillations are observed that decay on a timescale of ~1 ms, which is an approximate measure of the nuclear T_2 time. The decay probably originates from dipole–dipole coupling of the nuclear spin to surrounding paramagnetic electronic defects and nuclear spin impurities. The timescale of the decay arising from coupling to the naturally abundant ^{13}C lattice spins can be estimated to be ~10 ms using observations of the T_2^* times of ^{13}C spin ensembles in diamond[23]. Note that in this case of a central ^{13}C spin, the coupling to the ^{13}C lattice spins is a spin diffusion mechanism. Given this estimate, coupling to electronic defects within the nanowires, such as vacancy and interstitial-related defects created by the large strain in the nanowires, or to surface defects and impurities probably accounts for the slightly faster decay observed. To increase the coherence time in the future, dipole interactions between the ^{13}C nuclei can be efficiently removed by homonuclear decoupling schemes[10,24–26], and interactions with paramagnetic electronic defects can be reduced by isolating ST1 defects in the bulk crystal.

The defect spin system presented in this work holds promise for applications in room-temperature solid-state nuclear spin memories and quantum registers with ultralong spin coherence times. Such a device could be used as a memory in integrated hybrid quantum systems[14,15] or as a solid-state quantum token[10]. For such applications, coherence times on the order of seconds or hours are desirable. Because of its spin-free ground state, the system presented here is a promising candidate for achieving such long coherence times by homonuclear dynamical decoupling, such as in NMR sequences BLEW[24], FSLG[25], MREV[26]. An increase in the nuclear spin coherence time by several orders of magnitude is expected, as has been achieved recently with a single ^{13}C nuclear spin coupled to a single NV centre[10].

Methods

Polarization and readout of the triplet spin state. A long intense laser pulse was applied to prepare the system as a spin-polarized state of the triplet level. The intensity and length of the pulse were chosen so that the optical transition was saturated and steady-state fluorescence was reached during the pulse. In this way, the majority of the population was transferred to the slowly decaying triplet sublevel, while the two other triplet levels and the ground and excited states remained nearly empty. The laser pulse was followed by a short idle time (~50 ns) to allow any residual population of the excited state to decay.

To read out the triplet spin state, the fluorescence was recorded during a laser pulse that was identical to the preparation pulse. Decaying fluorescence response curves were observed that encode the triplet populations. In particular, the fluorescence counts summed over a window at the beginning of the response profiles are proportional to the three triplet spin populations. This fluorescence was plotted in Figs 3 and 4. In all data shown, a 200 ns integration window was used.

Polarization and readout of the nuclear spin. The nuclear spin was initialized by applying a long (10 μs) laser pulse (duration longer than several triplet lifetimes) followed by an idle time (20 μs) to ensure that the triplet population had fully decayed to the electronic ground state before any nuclear spin manipulation. The readout consisted of a second laser pulse with simultaneous detection of the fluorescence, as for the electron spin manipulation, except that a longer (8 μs) integration window was used to accumulate fluorescence contrast. As before, the integrated fluorescence encodes the spin state.

Specification of measurement uncertainties. For the excited-state lifetime, triplet-state population and decay rates, ESR resonance frequencies and line widths, electron and nuclear spin Rabi oscillations and nuclear spin signal contrast, the specified uncertainties are standard deviations of the model parameters (see text and figure captions for the respective model functions) obtained from maximum-likelihood estimation, which originated from the Poissonian distributed shot noise of the single photon counts (see Supplementary Section S4.2 for details on the multi-exponential fits). For the magnetic field calibration and g-factor of the ST1 electron spin, specified uncertainties are standard deviations originating from the uncertainty of the magnetic field calibration via nearby NV^- centres (Supplementary Section S5).

Received 19 February 2013; accepted 7 May 2013; published online 23 June 2013

References

1. Ladd, T. D. *et al.* Quantum computers. *Nature* **464,** 45–53 (2010).
2. Koehl, W. F., Buckley, B. B., Heremans, F. J., Calusine, G. & Awschalom, D. D. Room temperature coherent control of defect spin qubits in silicon carbide. *Nature* **479,** 84–87 (2011).
3. Morton, J. J. L. *et al.* Solid-state quantum memory using the ^{31}P nuclear spin. *Nature* **455,** 1085–1088 (2008).
4. Dutt, M. V. G. *et al.* Quantum register based on individual electronic and nuclear spin qubits in diamond. *Science* **316,** 1312–1316 (2007).
5. Neumann, P. *et al.* Single-shot readout of a single nuclear spin. *Science* **329,** 542–544 (2010).
6. Steger, M. *et al.* Quantum information storage for over 180 s using donor spins in a ^{28}Si 'semiconductor vacuum'. *Science* **336,** 1280–1283 (2012).
7. Pla, J. J. *et al.* High-fidelity readout and control of a nuclear spin qubit in silicon. *Nature* **496,** 334–338 (2013).
8. Neumann, P. *et al.* Multipartite entanglement among single spins in diamond. *Science* **320,** 1326–1329 (2008).
9. Filidou, V. *et al.* Ultrafast entangling gates between nuclear spins using photoexcited triplet states. *Nature Phys.* **8,** 1–5 (2012).
10. Maurer, P. C. *et al.* Room-temperature quantum bit memory exceeding one second. *Science* **336,** 1283–1286 (2012).
11. Akhtar, W. *et al.* Coherent storage of photoexcited triplet states using ^{29}Si nuclear spins in silicon. *Phys. Rev. Lett.* **108,** 1–5 (2012).
12. Brennecke, F., Ritter, S., Donner, T. & Esslinger, T. Cavity optomechanics with a Bose–Einstein condensate. *Science* **322,** 235–238 (2008).
13. Brown, K. R. *et al.* Coupled quantized mechanical oscillators. *Nature* **471,** 196–199 (2011).
14. Zhu, X. *et al.* Coherent coupling of a superconducting flux qubit to an electron spin ensemble in diamond. *Nature* **478,** 221–224 (2011).
15. Kubo, Y. *et al.* Strong coupling of a spin ensemble to a superconducting resonator. *Phys. Rev. Lett.* **105,** 1–4 (2010).
16. Babinec, T. M. *et al.* A diamond nanowire single-photon source. *Nature Nanotech.* **5,** 195–199 (2010).
17. Epstein, R. J., Mendoza, F. M., Kato, Y. K. & Awschalom, D. D. Anisotropic interactions of a single spin and dark-spin spectroscopy in diamond. *Nature Phys.* **1,** 94–98 (2005).
18. Kurtsiefer, C., Mayer, S., Zarda, P. & Weinfurter, H. Stable solid-state source of single photons. *Phys. Rev. Lett.* **85,** 290–293 (2000).
19. Zaitsev, A. M. *Optical Properties of Diamond: A Data Handbook* (Springer, 2001).
20. Carrington, A. & McLachlan, A. D. *Introduction to Magnetic Resonance with Applications to Chemistry and Chemical Physics* (Harper & Row, 1967).
21. Jacques, V. *et al.* Dynamic polarization of single nuclear spins by optical pumping of nitrogen-vacancy color centers in diamond at room temperature. *Phys. Rev. Lett.* **102,** 7–10 (2009).
22. Colpa, J. P. & Stehlik, D. Optical nuclear polarization as a consequence of the non-crossing rule (level-anti-crossing). *Chem. Phys.* **21,** 273–288 (1977).
23. Hoch, M. & Reynhardt, E. Nuclear spin-lattice relaxation of dilute spins in semiconducting diamond. *Phys. Rev. B* **37,** 9222–9226 (1988).
24. Burum, D., Linder, M. & Ernst, R. Low-power multipulse line narrowing in solid-state NMR. *J. Magn. Reson. (1969)* **44,** 173–188 (1981).
25. Bielecki, A., Kolbert, A. C. & Levitt, M. H. Frequency-switched pulse sequences: homonuclear decoupling and dilute spin NMR in solids. *Chem. Phys. Lett.* **155,** 341–346 (1989).
26. Rhim, W-K. Enhanced resolution for solid state NMR. *J. Chem. Phys.* **58,** 1772 (1973).

Acknowledgements

The authors acknowledge support from the DFG (Forschergruppe 1493 and SFB/TR21) as well as the EU (ERC grant SQUTEC and FP7 grants DIAMANT and QINVC). B.H. acknowledges support from HQOC. The authors thank M. Sellars, P. Hemmer, P. Neumann, R. Kolesov, R. Stöhr and C. Burk for discussions.

Author contributions

S.L., H.F. and J.W. designed the experiments. S.L., M.W., T.R., T.B., S.Y., M.E., P.S. and H.F. performed the experiments. S.L., M.W., M.D. and H.F. analysed the data. B.H. and M.L. fabricated the nanopillars. M.D., Z.B., A.G. and N.M. provided theoretical support. All authors discussed the data and commented on the manuscript. S.L., M.D., H.F. and J.W. wrote the paper.

Additional information

Supplementary information is available in the online version of the paper. Reprints and permissions information is available online at www.nature.com/reprints. Correspondence and requests for materials should be addressed to M.W.D. and H.F.

Competing financial interests

The authors declare no competing financial interests.